Chemical Science

ROYAL SOCIETY OF CHEMISTRY

EDGE ARTICLE

View Article Online
View Journal | View Issue

Cite this: *Chem. Sci.*, 2024, **15**, 18832

All publication charges for this article have been paid for by the Royal Society of Chemistry

Received 31st August 2024
Accepted 21st October 2024

DOI: 10.1039/d4sc05849f

rsc.li/chemical-science

Molecular cylinders with donor–acceptor structure and swinging motion†

Ke Li,[a] Satoshi Yoshida,[b] Ryo Yakushiji,[b] Xingchi Liu,[a] Chang Ge,[a] Zhuofan Xu,[a] Yong Ni,[d] Xiaonan Ma, [a] Jishan Wu, [e] Sota Sato *[bc] and Zhe Sun *[a]

The construction of three-dimensional nanocarbon structures with well-defined molecular dynamics is a challenging yet rewarding task in material science and supramolecular chemistry. Herein, we report the synthesis of two highly defective, nitrogen-doped molecular cylinders, namely **MC1** and **MC2**, with a length of 1.4 nm and 2.7 nm, respectively. These molecular cylinders are constructed by connecting the cycloparaphenylene endcaps and fused aromatic pillars using a cyclocondensation reaction, affording a distinct donor–acceptor structure. An X-ray crystallographic analysis reveals a tilted cylindrical shape for **MC1**, and nuclear magnetic resonance spectroscopy and calculations indicate the occurrence of a dynamic swinging motion in solution. The elongation of conjugation in the cylinders attenuates the charge transfer character in the first excited state, resulting in remarkable length-dependent photophysical properties.

Introduction

Complex three-dimensional (3D) nanocarbon structures with dynamic motions are intriguing yet challenging synthetic targets.[1–3] In particular, controlling molecular motions has led to molecular machines as a flourishing research field,[4–9] whereas the restriction of molecular motions often produce structurally unique 3D organic architectures, such as cages,[10,11] belts,[12–15] Möbius strips,[16–19] and interlocked systems.[20–23] The creation of distinctive molecular topologies is often associated with the emergence of chirality,[24–26] unique optoelectronic properties,[27] and encapsulation capabilities,[28,29] which stimulates the development of synthetic chemistry,[30,31] material science,[32] and supramolecular chemistry.[33] Among the 3D organic motifs, molecular cylinders are particularly attractive, and their construction represents a formidable task. Using phenine and porphyrin as building blocks, Isobe[34] and Anderson[35] prepared nanometer size phenine cylinders and porphyrin cylinders, respectively, using meticulously designed synthetic methods. However, the rational synthesis, structural elucidation, and investigation of molecular cylinders with dynamic motions remain challenging.

Recently, our group have developed a modular cyclocondensation approach for the π-lengthening of the cycloparaphenylenes (CPPs), which also allows for the incorporation of N atoms to produce donor–acceptor (D–A) structures with bright redshifted emission.[36] With CPP as an endcap and a N-doped aromatic moiety (NAM) as a pillar, a bridged dimeric CPP exhibiting distinctive flipping motion by virtue of the free rotating single bonds connecting the CPP and the NAM units was synthesized (Fig. 1a).[37] Following this design concept, we envisioned that the installation of an additional pillar at the opposite site would stop the flipping motion and force a persistent cylindrical shape. However, under this circumstance, the rotation of the single bonds connecting the CPP and the NAM units might not be fully restricted, resulting in a swinging motion. The molecular cylinders can be described by diameter (d), length (l), and angular displacement (θ) from the vertical equilibrium position (transition state shown in Fig. 1a), which is a phenomenon rarely observed in 3D nanocarbons.

Herein, we present the synthesis, structural elucidation, and photophysical properties of two discrete molecular cylinders, **MC1** and **MC2**, which possess tunable length, swinging dynamics, and length-dependent photophysical properties. These cylindrical molecules can be geometrically viewed as molecular fragments of N-doped (12,12)-carbon nanotubes (CNTs),[38] but they swing away from the perfect cylindrical shape in the crystalline state. The incorporation of both electron-

[a]*Institute of Molecular Plus, Department of Chemistry, Tianjin University and Haihe Laboratory of Sustainable Chemical Transformations, 92 Weijin Road, Tianjin, 300072, China. E-mail: zhesun@tju.edu.cn*

[b]*Integrated Molecular Structure Analysis Laboratory, Department of Applied Chemistry, School of Engineering, The University of Tokyo, 6-6-2 Kashiwanoha, Kashiwa-shi, Chiba 277-0882, Japan. E-mail: satosota@appchem.t.u-tokyo.ac.jp*

[c]*Institute for Molecular Science (IMS), 5-1 Higashiyama, Myodaiji, Okazaki, Aichi 444-8787, Japan*

[d]*Department of Chemistry, Southern University of Science and Technology, Shenzhen, Guangdong, 518055, China*

[e]*Department of Chemistry, National University of Singapore, 3 Science Drive 3, 117543, Singapore*

† Electronic supplementary information (ESI) available. CCDC 2363037. For ESI and crystallographic data in CIF or other electronic format see DOI: https://doi.org/10.1039/d4sc05849f

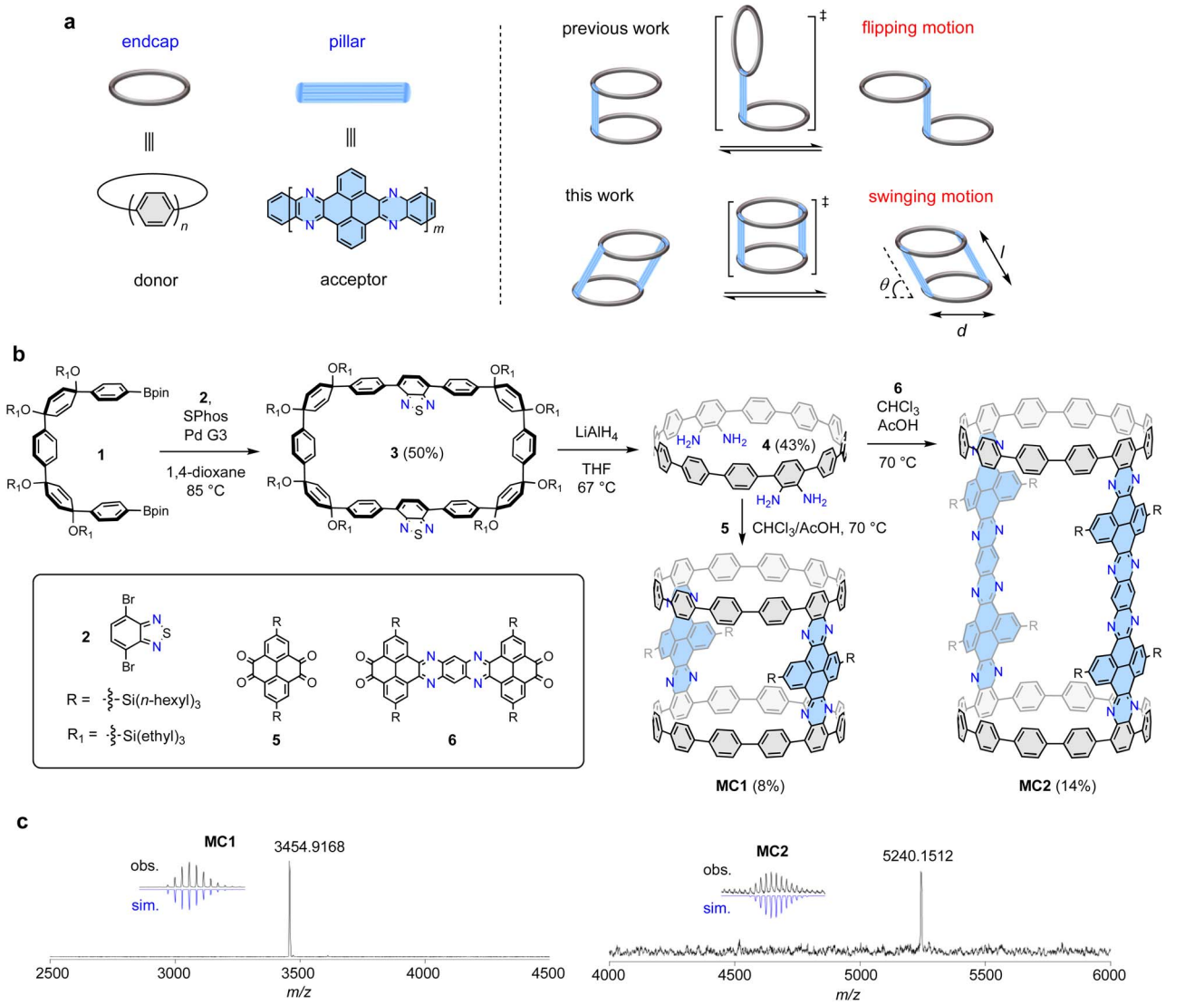

Fig. 1 Synthesis and structure of molecular cylinders **MC1** and **MC2**. (a) Molecular design and dynamic motion. (b) Synthesis of **MC1** and **MC2**. (c) High-resolution MALDI-TOF MS spectra.

donating CPP endcaps and electron-withdrawing NAM pillars into the molecular backbone leads to unique photophysical properties.[39]

Results and discussion

Design and synthesis

The construction of the proposed cylindrical structure hinges on a cyclocondensation reaction between a CPP tetraamine compound and an aromatic tetraketone compound. As shown in Fig. 1b, the synthesis of the key tetraamine intermediate started from a Suzuki macrocyclization reaction between the previously reported U-shaped compound **1** and dibromobenzothiadiazole **2**. The reaction concentration was carefully controlled at 1 mM to ensure an optimal reaction yield of 50% for macrocycle **3**. Subsequently, tetraamine intermediate **4** was obtained in 43% yield using a strategy previously developed by us, which involved a one-pot reductive aromatization–sulfur extrusion strategy using $LiAlH_4$.[37] A cyclocondensation reaction between **4** and tetraketone **5** afforded a mixture of cyclic and linear products, from which the desired product **MC1** was isolated in 8% yield using gel-permeable chromatography (GPC). Compound **5** was synthesized according to a reported method,[40] and a branched trihexylsilyl substituent was used to ensure a sufficient solubility for the target molecules. To maintain a highly diluted reaction environment that ensures macrocyclization is favored over undesired polymerization, **4** and **5** were simultaneously injected to a stirring solvent over a period of 2 h (see ESI† for details). Elongated tetraketone **6** was then prepared according to a reported method,[41] and the longer cylinder **MC2** was synthesized and isolated in 14% yield under the same reaction conditions and operational technique. The slightly higher yield of **MC2** than **MC1** may be due to its better solubility provided by branched trihexylsilyl substituent. The

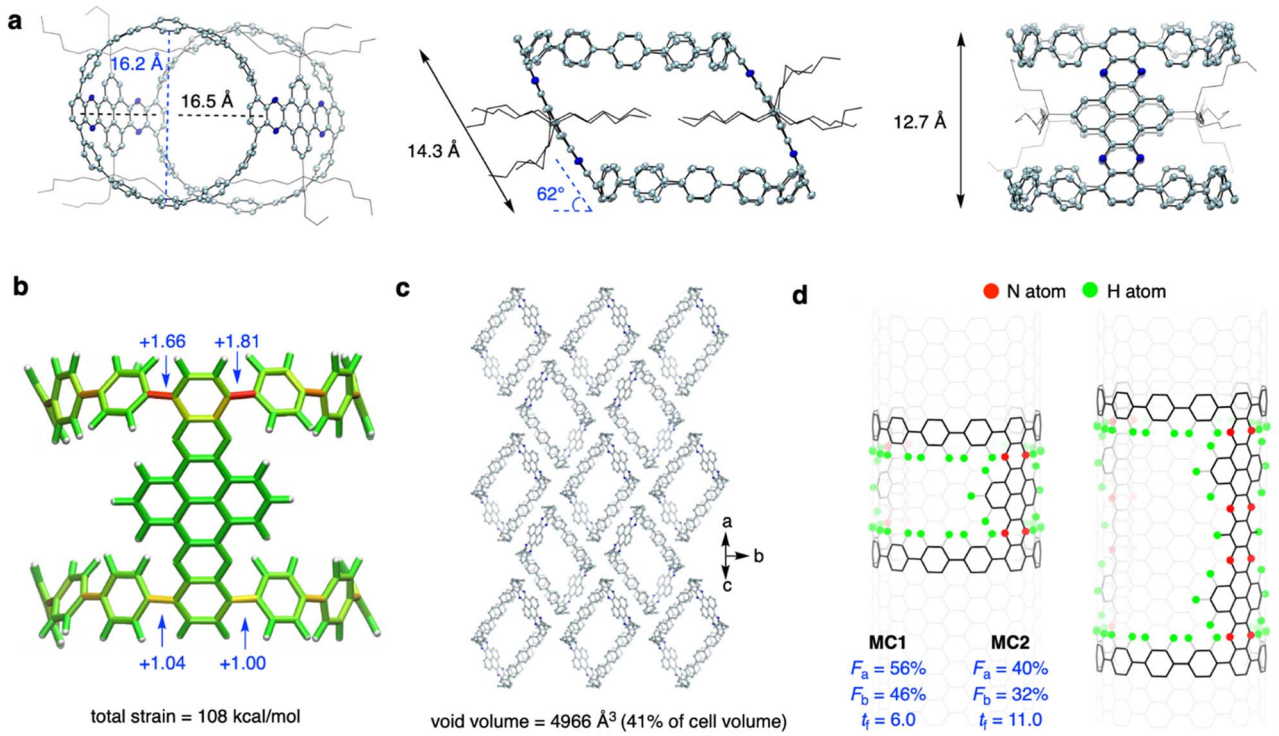

Fig. 2 Crystal structure of **MC1** and structural analysis. (a) Single crystal structures from top and side views. (b) StrainVis analysis of **MC1** without substituents from DFT optimization. (c) Packing structure of **MC1**. Aliphatic substituents and solvent molecules are omitted for clarity. (d) Mapping of **MC1** and **MC2** on CNT and the representative vector-based descriptions.

reaction sequence comprises only three linear steps from available starting materials; therefore, this concise synthetic approach can be expected to be readily applicable to other tetraketones to produce a variety of cylinders. The molecular structures of **MC1** and **MC2** were unambiguously confirmed by means of X-ray crystallography and spectroscopy analyses (*vide infra*). The chemical compositions of **MC1** ($C_{248}H_{252}N_8Si_4$) and **MC2** ($C_{364}H_{420}N_{16}Si_8$) were confirmed *via* high-resolution matrixassisted laser desorption/ionization (MALDI) mass spectroscopy, which showed a mass/charge ratio (m/z) of 3454.9168 and 5240.1512, respectively, matching well with the theoretical values of 3454.9115 and 5240.1584 (Fig. 1c).

X-ray crystallographic analysis

Yellow prism crystals of **MC1** and red ellipsoidal crystals of **MC2** were obtained *via* slow diffusion of *n*-hexane into a $CHCl_3$ solution at −20 °C (Fig. S1†). However, the fragibility of the **MC2** crystals prevented us from performing X-ray crystallographic measurements, and the **MC1** crystal gave weak diffraction patterns on a conventional X-ray diffractometer. Fortunately, measurements could be performed on a monochromated X-ray beam at KEK PF BL-17A beamline, affording data with sufficient resolution. As shown in Fig. 2a, the crystal structure of **MC1** showed a tilted cylindrical shape (a parallelogram shape from the side view) of nanometer size with an averaged diameter (d) of 16.4 Å, a tilting angle (θ) of 62°, a length (l) of 14.3 Å, and a height (h) of 12.7 Å. Such a geometry is beneficial for alleviating the strain of the sterically congested aliphatic chains. The endcapping CPP unit exhibited a slight deviation from the cycle, and the torsional angles of the aryl rings ranged from 23° to 51° (Fig. S2†). The decrease in symmetry from a perfect cylinder to a tilted cylinder also reduced the volume from 2308 Å^3 ($\theta = 90°$) to 2031 Å^3 ($\theta = 62°$) (Fig. S3†). Measurement of the π-orbital axis vectors (POAV)[42] indicated that the ipso-carbons have a structural deformation from planarity, with POAV values ranging from 2.79° to 3.88° (Fig. 2a and S4†). These values are larger than those of [12]CPP (averaged at 2.7°),[43] suggesting a more deformed CPP structure when confined into the tilted cylinder. The POAV values are slightly larger for the upper site (with acute angle of the parallelogram) than for the bottom site (with obtuse angle of the parallelogram), which is in agreement with the strain energies obtained by performing a StrainVis analysis (Fig. 2b),[44] and can be attributed to the intrusion of the NAM pillar into the cavity of the cylinder. The total strain energy calculated from the crystal structure was 108 kcal mol^{-1}, which is much lower than the strain energy of 281 kcal mol^{-1} for the perfect cylinder (Fig. S5†).

The **MC1** molecules were packed in the $P2_1/c$ space group (Table S1†), in which the cylinders assembled in a top-to-side fashion with the electron-rich CPP endcaps located spatially close to the electron-withdrawing NAM pillar (Fig. 2c and S6†). This packing mode is different from that of Isobe's cylinders[34] with a layered stacking of molecules, which could be ascribed to the unique D–A structure of **MC1**. The intercylinder interactions are mainly CH–π and π–π interactions between the donor and acceptor parts, and the aliphatic chains of the adjacent

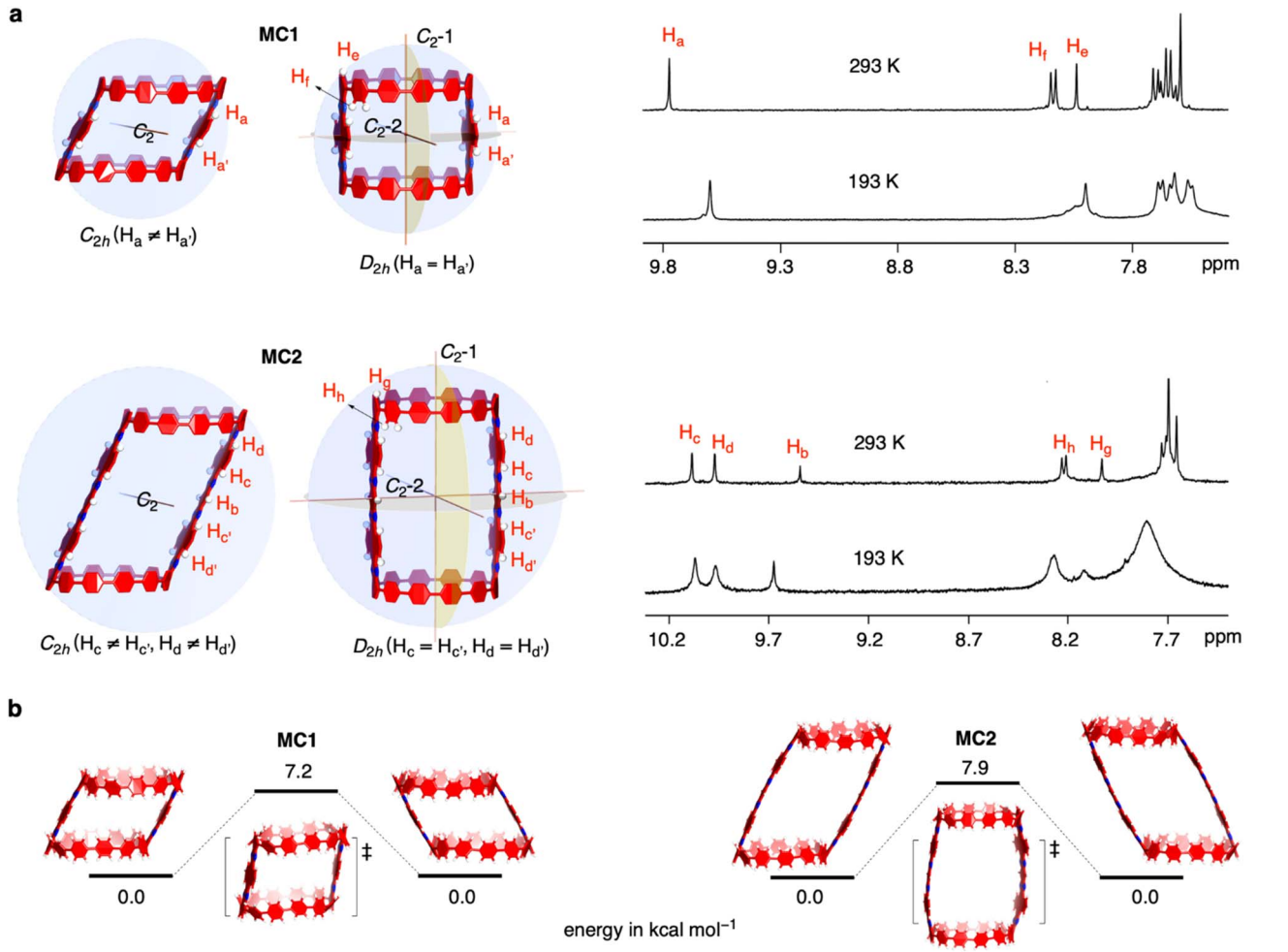

Fig. 3 NMR spectra and DFT calculations. (a) Variable temperature NMR spectra of **MC1** and **MC2** measured in dichloromethane-d_2/CS_2 and **MC2** measured in tetrahydrofuran-d_8, respectively. Illustrative structures with different symmetries are shown. (b) Calculated stationary and transition state structures for **MC1** and **MC2**.

cylinders and the hexane solvent molecules fill up the cavity of the central molecule (Fig. S6†). The analysis of the interior and interstitial void space resulted in a void volume of 4966 Å^3, which occupies 41% of the cell volume (Fig. 2c). Owing to its porous nature, the **MC1** crystal could find application in guest adsorption and catalysis.[45]

Then, we analyzed the defective nature and N-doping of **MC1** and **MC2** using the geometric measures for finite nanotube molecules developed by Isobe *et al.*[46] Theoretically, the perfect upright cylinders can be mapped into the (12,12)-CNT structure, and the vector indices of length index (t_f), atom-filling index (F_a), and bond-filling index (F_b) can be applied. The t_f values measures the length of the cylinder, and the F_a and F_b values quantify the occupancy of atoms and bonds of the cylinder in the mother CNT structure, which determines the defectiveness. As shown in Fig. 2d, the F_a values of **MC1** and **MC2** are 56% and 40% and F_b values of **MC1** and **MC2** are 46% and 32%, respectively, which are much smaller than those of the most defective finite nanotube molecule reported to date (F_a = 67% and F_b = 57%),[34] revealing that **MC1** and **MC2** possess a highly hollow structure. The t_f values of **MC1** and **MC2** are 6.0 and 11.0, respectively, which correspond to an actual length of 14.9 Å and 27.4 Å by multiplying the lattice constant, in consistent with the value obtained from the crystal structure. Note that the value of 11.0 for **MC2** exceeds that of the longest finite nanotube molecule reported (t_f = 7.0). Taken together, these results indicate that the molecular cylinder **MC2** is the longest, most defective finite nanotube molecule synthesized so far. In addition, using an oblique coordinate system,[47] the positions of 8 nitrogen atoms in **MC1** and 16 nitrogen atoms in **MC2** can be pinpointed (Fig. S7†).

Solution-phase structure and dynamics

The solution-phase structures of **MC1** and **MC2** were determined using nuclear magnetic resonance (NMR) spectroscopy. The introduction of solubilizing alkyl chains allowed obtaining well-resolved ^{1}H NMR signals at 293 K. A simple, symmetric spectral pattern was observed for both **MC1** and **MC2**, in which the protons at the upper (H_a, H_c, H_d) are equivalent with those at the bottom (H_a', H_c', H_d'), inconsistent with a C_{2h} symmetric

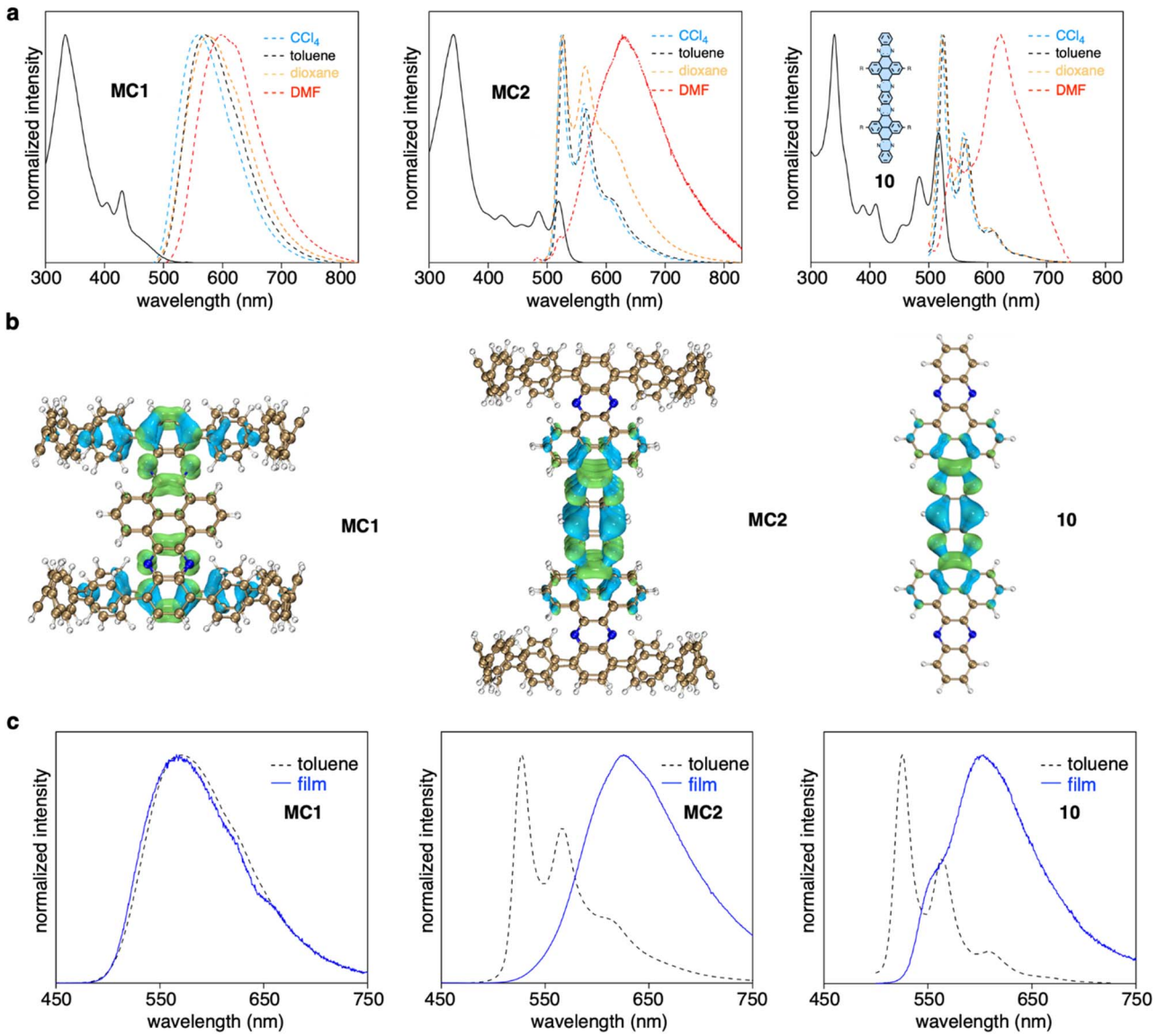

Fig. 4 Photophysical properties. (a) UV-vis absorption (solid line) in toluene and fluorescence (dashed line) spectra of **MC1**, **MC2**, and **10**. (b) Electron–hole analysis of the $S_0 \rightarrow S_1$ excitation. Blue and green regions denote hole and electron distributions, respectively (isovalue = 0.001). (c) Fluorescence spectra measured in toluene solution and in the film state.

tilted cylinder structure observed in the crystalline state (Fig. 3a). This observation suggests that the C_{2h} tilted cylinder structure is not persistent in the solution phase; instead, the molecule swing back and forth like a pendulum on the NMR time scale to give a time-averaged D_{2h} structure. Lowering the temperature led to broadening of the signals, implying a slow-down of the dynamic motion (Fig. 3a and S8, S9†). Unfortunately, the $H_a/H_b/H_c$ and $H_a'/H_b'/H_c'$ protons of the C_{2h} structure could not be distinguished even at the instrumental temperature limit of 193 K. The proton signals on the NAM pillar could be assigned using two-dimensional COSY and NOESY spectra (Fig. S10 and S11†). In general, the protons from the NAM panel appeared at the relatively lower field than those from the CPP units due to a considerable deshielding from the fused aromatic moiety.

Next, we investigated the swinging dynamics *via* theoretical calculations. First, we performed a torsional scan analysis on the energetics by freezing the dihedral angles between CPP and NAM at the semiempirical PM6 level to locate the transition state (TS, Fig. S12†),[48] and more precise energetics were obtained by performing geometry optimizations with density functional theory (DFT) calculations at the M062X/6-31G(d,p) level (Fig. 3b). TS structures with nearly upright geometries were found with an activation energy of 7.2 kcal mol^{-1} for **MC1** and 7.9 kcal mol^{-1} for **MC2**, respectively. These values are lower than the activation energy for the ring-flipping of the single-pillar CPP dimer (10.1 kcal mol^{-1}), which is consistent with a coalescence temperature close or below 193 K, as observed in variable-temperature NMR measurements.

Photophysical properties

MC1 and **MC2** exhibited distinct length-dependent photophysical properties. The absorption spectra of **MC1** and **MC2** displayed a prominent peak at around 340 nm, with shoulder peaks extending to 500 nm for **MC1** and 550 nm for **MC2** (Fig. 4a). However, time-dependent DFT calculations suggested that the seemingly similar absorption spectra possessed different origins. For **MC1**, the maximum absorption (λ_{max}) at 333 nm corresponds to the electronic transitions from HOMO−1 to LUMO+8/LUMO+9, and the shoulder peaks at lower energy regime stem from the partially allowed HOMO to LUMO transition (Fig. S13 and Table S2†). The occupied and unoccupied molecular orbitals involved in the transitions are spatially separated and localized at the CPP and NAM units, respectively, similar to our previously reported D–A nanohoops.[36] In contrast, the λ_{max} and shoulder peaks of **MC2** are due to HOMO−6 to LUMO+7/HOMO−7 to LUMO+6 and HOMO−8 to LUMO/HOMO−9 to LUMO+1 transitions, with the orbitals being exclusively distributed on the NAM unit (Fig. S14 and Table S3†). This result suggests that the NAM moiety serves as a chromophore for **MC2**, whereas the contribution from CPP is negligible. The absorption spectrum of substructure **10**, which was synthesized for comparison, was very similar to that of **MC2**, confirming that NAM is responsible for the observed absorption of **MC2**.

The fluorescence spectra of **MC1** and **MC2** were also distinct. A clear bathochromic shift from 560 to 600 nm was observed for **MC1** when the fluorescence was measured in solvents with increased polarity (Fig. 4a). The E_T (30) plot gave a good linearity, which suggests a positive solvatofluorochromism, *i.e.* the dipole moment of S_1 is higher than S_0 state (Fig. S15†).[49] Meanwhile, **MC2** showed typical LE fluorescence spectra with vibronic progression in CCl_4, toluene, and dioxane, whiledisplayed a redshifted spectrum in *N*,*N*-dimethylformamide (DMF). This behavior is also reminiscent of the solvent dependence of **10**. A quantitative electron–hole analysis[50] on the critical $S_0 \rightarrow S_1$ excitation was performed to gain further insight into the observed emission (Fig. 4b, S16, and Table S4†). Both CPP and NAM units of **MC1** were found to participate in S_1 (CT) excitation, whereas the S_1 excitation was confined on the central NAM moiety for **MC2** and **10**. As a result, the S_1 state of **MC1** possessed 41% of charge transfer (CT) contribution and 59% of local excitation (LE) contribution, whereas only LE contributed to the S_1 state of **MC2** and **10**. This explains the existence of solvatofluorochromism of **MC1** and the spectral featuring of vibronic progression for **MC2**.[51] The anomalous spectra in DMF can be explained in terms of the aggregation caused by intermolecular interactions in a polar solvent.[52] This hypothesis was further supported by measuring the fluorescence in toluene solution and in the film state (Fig. 4c). In both cases, the spectral pattern was almost identical for **MC1**, but a redshifted behavior from solution to the film state was observed for **MC2** and **10**. The fluorescence quantum yield (Φ) of **MC1** was determined to be 63% in toluene (Fig. S17†), which is surprisingly high for a nanometer-sized molecular cylinder. This result, together with the unique D–A structure and length dependence, suggests that such molecular cylinders are good candidates for the exploration of new photophysical mechanisms and applications.[53]

Conclusions

In summary, two N-doped molecular cylinders, **MC1** and **MC2**, with a well-defined D–A structure and tunable length were synthesized using cyclocondensation as a key macrocyclization approach. Their structures can be viewed as molecular fragments of N-doped (12,12)-CNTs. An X-ray crystallographic analysis revealed the tilted cylindrical geometry and porous nature of the crystal packing, and a swinging motion was revealed in solution by spectroscopic and computational methods. The molecular cylinders exhibited unique length-dependent photophysical properties. Moreover, the shorter cylinder possessed considerable CT characteristics, and the elongation of the aromatic pillar weakens the contribution from the CPP units. The molecules reported here may serve as discrete molecular models for the understanding of the effect of heteroatom doping in CNTs,[54,55] and open a new avenue for the development of cylindrical shaped molecular hosts, dynamic systems, and functional materials.[56]

Data availability

The data supporting this article have been included as part of the ESI.†

Author contributions

K. L. and Z. S. conceived the design. Z. S., S. S., and J. W. supervised the project. K. L., X. L., and C. G. performed the synthesis, compound characterization and data analysis. S. Y., R. Y., and S. S. performed the crystallographic studies. All authors analyzed and discussed the results, and K. L. and Z. S. wrote the manuscript.

Conflicts of interest

There are no conflicts to declare.

Acknowledgements

Z. S. acknowledge financial support from National Natural Science Foundation of China (Grant No. 22222110, 22371206) and the Haihe Laboratory of Sustainable Chemical Transformations (24HHWCSS00009). S. S. acknowledges experimental support from KEK Photon Factory Program Advisory Committee (Grant No. 2023G604) for the use of BL-17A beamline.

Notes and references

1 L. Feng, R. D. Astumian and J. F. Stoddart, *Nat. Rev. Chem*, 2022, **6**, 705–725.

2 X. Wang, F. Jia, L.-P. Yang, H. Zhou and W. Jiang, *Chem. Soc. Rev.*, 2020, **49**, 4176–4188.
3 Y. Segawa, H. Ito and K. Itami, *Nat. Rev. Mater.*, 2016, **1**, 15002.
4 R. A. Bissell, E. Córdova, A. E. Kaifer and J. F. Stoddart, *Nature*, 1994, **369**, 133–137.
5 L. Feng, Y. Qiu, Q.-H. Guo, Z. Chen, J. S. W. Seale, K. He, H. Wu, Y. Feng, O. K. Farha, R. D. Astumian and J. F. Stoddart, *Science*, 2021, **374**, 1215–1221.
6 L. Zhang, Y. Qiu, W.-G. Liu, H. Chen, D. Shen, B. Song, K. Cai, H. Wu, Y. Jiao, Y. Feng, J. S. W. Seale, C. Pezzato, J. Tian, Y. Tan, X.-Y. Chen, Q.-H. Guo, C. L. Stern, D. Philp, R. D. Astumian III, W. A. Goddard and J. F. Stoddart, *Nature*, 2023, **613**, 280–286.
7 N. P. M. Huck, W. F. Jager, B. de Lange and B. L. Feringa, *Science*, 1996, **273**, 1686–1688.
8 N. Koumura, R. W. J. Zijlstra, R. A. van Delden, N. Harada and B. L. Feringa, *Nature*, 1999, **401**, 152–155.
9 P. Štacko, J. C. M. Kistemaker, T. van Leeuwen, M.-C. Chang, E. Otten and B. L. Feringa, *Science*, 2017, **356**, 964–968.
10 Q.-F. Sun, J. Iwasa, D. Ogawa, Y. Ishido, S. Sato, T. Ozeki, Y. Sei, K. Yamaguchi and M. Fujita, *Science*, 2010, **328**, 1144–1147.
11 Y. Ni, T. Y. Gopalakrishna, H. Phan, T. Kim, T. S. Herng, Y. Han, T. Tao, J. Ding, D. Kim and J. Wu, *Nat. Chem.*, 2020, **12**, 242–248.
12 G. Povie, Y. Segawa, T. Nishihara, Y. Miyauchi and K. Itami, *Science*, 2017, **356**, 172–175.
13 K. Y. Cheung, K. Watanabe, Y. Segawa and K. Itami, *Nat. Chem.*, 2021, **13**, 255–259.
14 Y. Han, S. Dong, J. Shao, W. Fan and C. Chi, *Angew. Chem., Int. Ed.*, 2021, **60**, 2658–2662.
15 K. Y. Cheung, S. Gui, C. Deng, H. Liang, Z. Xia, Z. Liu, L. Chi and Q. Miao, *Chem*, 2019, **5**, 838–847.
16 W. Fan, T. M. Fukunaga, S. Wu, Y. Han, Q. Zhou, J. Wang, Z. Li, X. Hou, H. Wei, Y. Ni, H. Isobe and J. Wu, *Nat. Synth.*, 2023, **2**, 880–887.
17 Y. Segawa, T. Watanabe, K. Yamanoue, M. Kuwayama, K. Watanabe, J. Pirillo, Y. Hijikata and K. Itami, *Nat. Synth.*, 2022, **1**, 535–541.
18 D. Ajami, O. Oeckler, A. Simon and R. Herges, *Nature*, 2003, **426**, 819–821.
19 Y. Tanaka, S. Saito, S. Mori, N. Aratani, H. Shinokubo, N. Shibata, Y. Higuchi, Z. S. Yoon, K. S. Kim, S. B. Noh, J. K. Park, D. Kim and A. Osuka, *Angew. Chem., Int. Ed.*, 2008, **47**, 681–684.
20 Y. Segawa, M. Kuwayama, Y. Hijikata, M. Fushimi, T. Nishihara, J. Pirillo, J. Shirasaki, N. Kubota and K. Itami, *Science*, 2019, **365**, 272–276.
21 J. H. May, J. M. Van Raden, R. L. Maust, L. N. Zakharov and R. Jasti, *Nat. Chem.*, 2023, **15**, 170–176.
22 Y.-Y. Fan, D. Chen, Z.-A. Huang, J. Zhu, C.-H. Tung, L.-Z. Wu and H. Cong, *Nat. Commun.*, 2018, **9**, 3037.
23 A. Bu, Y. Zhao, H. Xiao, C.-H. Tung, L.-Z. Wu and H. Cong, *Angew. Chem., Int. Ed.*, 2022, **61**, e202209449.
24 S. Hitosugi, W. Nakanishi, T. Yamasaki and H. Isobe, *Nat. Commun.*, 2011, **2**, 492.
25 Y. Tian, Y. Guo, X. Dong, X. Wan, K.-H. Cheng, R. Chang, S. Li, X. Cao, Y.-T. Chan and A. C.-H. Sue, *Nat. Synth.*, 2023, **2**, 395–402.
26 S. Sato, A. Yoshii, S. Takahashi, S. Furumi, M. Takeuchi and H. Isobe, *Proc. Natl. Acad. Sci. U. S. A.*, 2017, **114**, 13097–13101.
27 X. Zhang, H. Liu, G. Zhuang, S. Yang and P. Du, *Nat. Commun.*, 2022, **13**, 3543.
28 T. Iwamoto, Y. Watanabe, T. Sadahiro, T. Haino and S. Yamago, *Angew. Chem., Int. Ed.*, 2011, **50**, 8342–8344.
29 E. Ubasart, O. Borodin, C. Fuertes-Espinosa, Y. Xu, C. García-Simón, L. Gómez, J. Juanhuix, F. Gándara, I. Imaz, D. Maspoch, M. von Delius and X. Ribas, *Nat. Chem.*, 2021, **13**, 420–427.
30 S. Hitosugi, A. Matsumoto, Y. Kaimori, R. Iizuka, K. Soai and H. Isobe, *Org. Lett.*, 2014, **16**, 645–647.
31 E. Kayahara, T. Hayashi, K. Takeuchi, F. Ozawa, K. Ashida, S. Ogoshi and S. Yamago, *Angew. Chem., Int. Ed.*, 2018, **57**, 11418–11421.
32 E. J. Leonhardt and R. Jasti, *Nat. Rev. Chem*, 2019, **3**, 672–686.
33 Y. Xu and M. von Delius, *Angew. Chem., Int. Ed.*, 2020, **59**, 559–573.
34 Z. Sun, K. Ikemoto, T. M. Fukunaga, T. Koretsune, R. Arita, S. Sato and H. Isobe, *Science*, 2019, **363**, 151–155.
35 M. Hoffmann, C. J. Wilson, B. Odell and H. L. Anderson, *Angew. Chem., Int. Ed.*, 2007, **46**, 3122–3125.
36 H. Deng, Z. Guo, Y. Wang, K. Li, Q. Zhou, C. Ge, Z. Xu, S. Sato, X. Ma and Z. Sun, *Chem. Sci.*, 2022, **13**, 14080–14089.
37 K. Li, Z. Xu, H. Deng, Z. Zhou, Y. Dang and Z. Sun, *Angew. Chem., Int. Ed.*, 2021, **60**, 7649–7653.
38 K. Ikemoto, S. Yang, H. Naito, M. Kotani, S. Sato and H. Isobe, *Nat. Commun.*, 2020, **11**, 1807.
39 M. Hermann, D. Wassy and B. Esser, *Angew. Chem., Int. Ed.*, 2021, **60**, 15743–15766.
40 S. More, R. Bhosale, S. Choudhary and A. Mateo-Alonso, *Org. Lett.*, 2012, **14**, 4170–4173.
41 A. Mateo-Alonso, N. Kulisic, G. Valenti, M. Marcaccio, F. Paolucci and M. Prato, *Chem.–Asian J.*, 2010, **5**, 482–485.
42 R. C. Haddon, *Pure Appl. Chem.*, 1986, **58**, 137–142.
43 Y. Segawa, S. Miyamoto, H. Omachi, S. Matsuura, P. Šenel, T. Sasamori, N. Tokitoh and K. Itami, *Angew. Chem., Int. Ed.*, 2011, **50**, 3244–3248.
44 C. E. Colwell, T. W. Price, T. Stauch and R. Jasti, *Chem. Sci.*, 2020, **11**, 3923–3930.
45 M.-H. Sun, S.-Z. Huang, L.-H. Chen, Y. Li, X.-Y. Yang, Z.-Y. Yuan and B.-L. Su, *Chem. Soc. Rev.*, 2016, **45**, 3479–3563.
46 T. Matsuno, H. Naito, S. Hitosugi, S. Sato, M. Kotani and H. Isobe, *Pure Appl. Chem.*, 2014, **86**, 489–495.
47 R. Saito, G. Dresselhaus and M. S. Dresselhaus, *Physical properties of carbon nanotubes*, Imperial College Press, London, 1998.
48 J. Xia, M. R. Golder, M. E. Foster, B. M. Wong and R. Jasti, *J. Am. Chem. Soc.*, 2012, **134**, 19709–19715.
49 C. Reichardt, *Chem. Rev.*, 1994, **94**, 2319–2358.
50 Z. Liu, T. Lu and Q. Chen, *Carbon*, 2020, **165**, 461–467.
51 W. Li, D. Liu, F. Shen, D. Ma, Z. Wang, T. Feng, Y. Xu, B. Yang and Y. Ma, *Adv. Funct. Mater.*, 2012, **22**, 2797–2803.

52 D. Wasserfallen, M. Kastler, W. Pisula, W. A. Hofer, Y. Fogel, Z. Wang and K. Müllen, *J. Am. Chem. Soc.*, 2006, **128**, 1334–1339.
53 H. Uoyama, K. Goushi, K. Shizu, H. Nomura and C. Adachi, *Nature*, 2012, **492**, 234–238.
54 P. Ayala, R. Arenal, M. Rümmeli, A. Rubio and T. Pichler, *Carbon*, 2010, **48**, 575–586.
55 M. Inagaki, M. Toyoda, Y. Soneda and T. Morishita, *Carbon*, 2018, **132**, 104–140.
56 U. H. F. Bunz, *Acc. Chem. Res.*, 2015, **48**, 1676–1686.